scientific reports

Check for updates

OPEN

Spatial mapping of influenza and coronavirus receptors in the respiratory and intestinal tract epithelium of beef cattle using advanced PixF image analysis

Ning-Chieh Twu[1,8], Yee Chuen Teoh[2,8], Curwen Pei Hong Tan[2,3], Riza Danudoro[2,3], Xiaoyi Cheng[4], Raquel Espin-Palazon[4], Todd Bell[5], Luis Giménez-Lirola[1], Ratul Chowdhury[3,6]✉ & Rahul Kumar Nelli[1,7]✉

Influenza A viruses (IAV) and coronaviruses (CoV) pose significant threats to various animal species, including cattle. Reports of SARS-CoV-2 infections and recent outbreaks of highly pathogenic avian influenza (HPAI H5N1) in dairy cattle highlight the need to understand receptor distributions critical for viral entry. This study investigates the spatial distribution of IAV and CoV receptors in bovine tissues using PixF, a novel and newly developed web-based image analysis tool. Respiratory (trachea and lung) and intestinal (small and large intestine) tissues from crossbred Holstein-Angus steers were analyzed. Lectin histochemistry staining with fluorescently labeled *Sambucus nigra* (SA α2,6-Gal receptors) and *Maackia amurensis* (SA α2,3-Gal receptors) identified IAV receptors, while coronavirus receptors ACE2, TMPRSS2, APN, DPP4, and CEACAM1 were assessed using indirect immunofluorescence. PixF provides an initial yet tailored image processing framework for quantifying and mapping receptor expression, revealing a predominance of SA α2,3-Gal receptors in epithelial regions, while SA α2,6-Gal receptors were confined to glandular tissues of the respiratory tract. Coronavirus receptors exhibited variable expression across tissues; TMPRSS2, APN, and DPP4 are highly expressed in the respiratory mucosal epithelium; ACE2, TMPRSS2, and DPP4 are highly expressed in the intestinal mucosal epithelium, while CEACAM1 is notably low across tissues. These findings demonstrate the potential utility of PixF, a simple prototypic fluorescence quantification tool customized for the use case detailed in this work, to provide a browser interface that prioritizes ease-of-use, enabling non-specialists to obtain essential quantification and spatial information quickly. PixF was utilized to elucidate receptor co-localization and enhance our understanding of host-pathogen interactions in cattle, offering a reproducible, accessible, and biologically informed analysis pipeline.

Keywords Sialic acid, ACE2, Influenza virus, Coronavirus, Respiratory tract, Intestinal tract, Beef cattle

Influenza and certain coronaviruses are highly contagious and have each led to significant pandemics[1,2]. Some coronaviruses cause enteric rather than respiratory infections in animals, leading to epidemics in livestock[3,4]. The economic impacts of influenza and coronavirus pandemics are substantial, with far-reaching global effects, as seen recently with the COVID-19 pandemic[5]. These zoonotic viruses can mutate and evolve rapidly, posing persistent human and animal health challenges. Additionally, both influenza and coronavirus strains infect a

[1]Department of Veterinary Diagnostic and Production Animal Medicine, Iowa State University, Ames, IA, USA. [2]Department of Computer Science, Iowa State University, Ames, IA, USA. [3]Nanovaccine Institute, Iowa State University, Ames, IA, USA. [4]Department of Genetics, Development and Cell Biology, Iowa State University, Ames, IA, USA. [5]Department of Veterinary Pathology, Iowa State University, Ames, IA, USA. [6]Department of Chemical and Biological Engineering, Iowa State University, Ames, IA 50011, USA. [7]Department of Veterinary Diagnostic and Production Animal Medicine, College of Veterinary Medicine, Iowa State University, 1907 ISU C Drive, VMRI#2, Ames, IA 50011, USA. [8]Ning-Chieh Twu and Yee Chuen Teoh have contributed equally to this work. ✉email: ratul@iastate.edu; rknelli@iastate.edu

broad range of animals, including marine and wild mammalian and avian species, some of which can act as reservoirs, facilitating viral persistence[6,7].

These RNA viruses are inherently error-prone during genome replication, leading to high mutation rates that foster adaptation to new species[8]. Another factor contributing to cross-species transmission is the presence of conserved viral receptors on host cells. For example, influenza viruses use sialic acids (SA) as receptors for cell attachment and entry. Influenza A viruses (IAVs) typically originating from avian species preferentially bind to SA receptors linked to galactose by an α2,3 linkage (SA α2,3-Gal), with a preference for SA α2,3-Gal-β (1–4) N-Acetylglucosamine (GlcNAc) in chickens and SA α2,3-Gal-β (1–3) N-Acetylgalactosamine (GalNAc) in ducks[9]. By contrast, IAVs from humans and classical swine isolates prefer SA receptors with an α2,6-galactose linkage (SA α2,6-Gal)[9–13]. Sialic acids also serve as potential receptors or co-receptors for other virus families, including *Coronaviridae* (SARS-CoV-2)[14], *Paramyxoviridae* (parainfluenza viruses), *Flaviviridae* (Zika virus)[15], *Picornaviridae* (murine norovirus)[16], *Reoviridae* (Rotavirus)[17], *Parvoviridae* (Adeno-associated virus)[18], Adenoviridae[19], *Papillomaviridae* (Human papillomavirus), *Polyomaviridae* (mouse polyomavirus)[20], *Caliciviridae* (Feline calicivirus)[21], and others.

In addition to SAs, coronaviruses utilize various host cell receptors such as angiotensin-converting enzyme 2 (ACE2)[22], aminopeptidase N (APN)[23], carcinoembryonic antigen-related cell adhesion molecule 1 (CEACAM1)[24], and dipeptidyl peptidase 4 (DPP4)[25]. These receptors play a critical role in enabling cross-species transmission[26].

Various staining and imaging techniques assess the distribution of virus receptors on host cells and tissues, with expression patterns varying by method. For example, dual staining with fluorescent dyes can complicate co-expression analysis, as overlapping signals may obscure molecule levels[27]. High image resolution is essential for images with co-localizing probes (e.g., with green and red emission), and confocal imaging offers the precision needed. Pixel-based analysis allows true co-localization by removing bleed-through and non-specific fluorescence from captured images.

This study developed a pixel-based fluorescence analysis tool for rapid image characterization called "PixF" to measure the spatial intensity of red and green emission at each locus in collected images. PixF enables on-the-fly splitting of individual red and green channels from co-expression data, effectively mapping per-molecule expression upon the tissue samples. PixF provides a potentially faster alternative to tools such as ImageJ while maintaining analytical quality. Additionally, PixF allows for 3D-bar plot visualization, where the x and y axes represent the spatial loci on tissue samples, and the z-axis displays absolute fluorescence intensity, empirically mapped to the RGB scale. These visualizations help identify differential molecule expression in specific tissue regions (e.g., epithelial lining), providing insights into infection and viral entry mechanisms. PixF is freely accessible as a web tool at https://pixf.onrender.com/, with source code available on GitHub at https://github.com/ChowdhuryRatul/pixf-channel-analysis.

PixF is not positioned as a replacement for exhaustive, annotation-heavy platforms like ImageJ, CellProfiler, or Imaris. Its primary objective is speed and accessibility for high-throughput, browser-based fluorescence quantification without requiring local installation or programming expertise. While detailed benchmarking may be warranted in future technical validations, the manuscript highlights that PixF achieves reliable quantification within seconds for hundreds of images. A task that typically requires hours using traditional tools. The emphasis is on delivering comparable outcomes for basic quantification tasks, not outperforming expert-level plugins in precision. PixF is being presented as a potential tool (pending development and detailed benchmarking) suited for rapid, exploratory analyses or large-scale tissue screening where real-time responsiveness is more valuable than maximal granularity.

Methods

Sample collection

Respiratory tract tissues (trachea and lung) and intestinal tissues (small and large intestine) from three healthy, 3-year-old, crossbred Holstein-Angus steers were included in this study. Samples were collected from the Iowa State University Meat Laboratory during the routine slaughtering process for meat. Tissues were fixed in 10% neutral buffered neutral formalin and then embedded in paraffin blocks. Sections were sliced at 4 µm thickness, transferred onto glass slides (VWR International, Radnor, PA, USA), and prepared for analysis. Lectin staining was used to demonstrate sialic acids, and an indirect immunofluorescence assay was used to detect coronavirus receptors.

For antigen retrieval, deparaffinized slides were treated with 10 mM sodium citrate buffer (pH 6.0; Millipore-Sigma, Burlington, MA, USA) at 96 °C for 30 min, then washed three times with Tris-buffered saline containing 0.1% Tween 20 (TBST; Millipore-Sigma).

Lectin staining

Plant lectins from *Sambucus nigra* (SNA), *Maackia amurensis* (MAL-I and MAL-II) were used to detect α2,6-linked SA, SA α2,3-Gal-β (1–4) GlcNAc and SA α2,3-Gal-β (1–3) GalNAc, respectively. To block non-specific binding, tissue sections were incubated with Carbo-Free™ Blocking Solution (Cat# SP-5040-125, Vector Laboratories, Burlingame, CA, USA) for 30 min at room temperature (21–22 °C). Endogenous biotin, biotin receptors, and streptavidin binding sites in tissues were blocked by incubating with biotin and streptavidin solutions (Cat# SP-2002, Vector Laboratories) for 10 min at room temperature.

The sections were then incubated overnight (16 h) at 4 °C in a humidified chamber with optimized concentrations of 10 µg/ml fluorescein isothiocyanate (FITC) labeled SNA (Cat# FL-1301-2, Vector Laboratories) or 10 µg/ml FITC labeled MAL I (Cat# FL-1311-2, Vector Laboratories), and 5 µg/ml MAL II (Cat# B-1265-1, Vector Laboratories). After three washes with TBST, the sections were incubated with 2 µg/ml streptavidin-DyLight 650 (Cat# 84547, Thermo Fisher Scientific, Waltham, MA, USA) for 2 h at 4 °C. Following

three additional washes with TBST, the sections were air-dried and mounted with ProLong™ Diamond Antifade Mountant containing 4',6-diamino-2-phenylindole, dihydrochloride (DAPI) (Cat# P36962, Thermo Fisher Scientific).

Immunofluorescence assay (IFA)

For SA detection, N-glycolylneuraminic acid (Neu5Gc) was targeted using a polyclonal chicken anti-Neu5Gc antibody Kit (Cat# 146901, BioLegend, San Diego, CA, USA) for IFA. The staining procedure followed a previously described protocol with minor modifications[28]. After deparaffinization and antigen retrieval via heat treatment, slides were incubated in Neu5Gc Assay Blocking Solution (1:40 dilution in TBST; Cat# 77294, BioLegend) for 30 min at room temperature. Following three washes with TBST, sections were incubated with 0.25 µg/ml anti-Neu5Gc antibody (diluted in Blocking Solution; Cat# 146903, BioLegend) for 1 h at room temperature in a humidified chamber. After three more washes with TBST, sections were incubated with 1 µg/ml FITC conjugated goat anti-chicken IgY secondary antibody (Cat# 410802, BioLegend) for 1 h at room temperature. Sections were air-dried and mounted with DAPI after three additional washes with TBST.

Likewise, coronavirus receptors, angiotensin-converting enzyme 2 (ACE2), transmembrane serine protease 2 (TMPRSS2), aminopeptidase N (APN), dipeptidyl peptidase 4 (DPP4), and carcinoembryonic antigen-related cell adhesion molecule 1 (CEACAM1) were assessed by IFA. Deparaffinized and heat-treated antigen retrieval sections were incubated with Animal-Free Blocker R.T.U (Cat# SP-5035, Vector Laboratories) for 30 min at room temperature, followed by incubation with optimized concentrations of primary antibodies: ACE2 (4 µg/ml, Cat# sc-390851, Santa Cruz Biotechnology, Dallas, TX, USA), TMPRSS2 (0.2 µg/ml; Cat# sc-515727, Santa Cruz Biotechnology), APN (0.16 µg/ml; Cat# sc-166105, Santa Cruz Biotechnology), CEACAM1 (4 µg/ml; Cat# sc-166453, Santa Cruz Biotechnology), and DPP4 (1:50 dilution; Cat# BOV2078, Washington State University Monoclonal Antibody Center, Pullman, WA, USA) overnight (16 h) at 4 °C. After three washes with TBST, sections were incubated with 15 µg/ml AffiniPure™ Donkey Anti-Mouse IgG (H + L) conjugated Alexa Fluor® 488 (Cat# 715-545-150, Jackson ImmunoResearch, West Grove, PA, USA) diluted in Animal-Free Blocker R.T.U, for 1 h at room temperature. Sections were washed three times with TBST, air-dried, and mounted with DAPI. All antibodies were previously verified in-silico (Supplementary Table S1) and in bovine kidney using immunohistochemistry (Supplementary Fig. S1).

Confocal laser scanning microscopy

Slides were cured in the dark for 24 h, and IFA images were captured using a 63x/1.40 oil objective by Zeiss LSM 700 Laser Scanning Confocal Microscope with Zen Black software version v14.0.27.201 (Carl Zeiss, Jena, Germany). For lectin staining, images were acquired with a 63x/1.40 oil objective on a Stellaris 5 STED Confocal Microscope using Leica Application Suite X (LAS X) software 1.4.7.28982 (Leica Microsystems Inc., Buffalo Grove, IL, USA; https://www.leica-microsystems.com/products/microscope-software/p/leica-las-x-ls/downloads/). All settings were calibrated against respective controls (e.g., secondary antibody controls, streptavidin-conjugated controls) for each staining technique and microscopy system. Images were captured as 1024 × 1024 pixels, with scale bars embedded on each image.

Image analysis using chromaticity in PixF

Mapping colorbars to chromaticity and fluorescence imaging bridges raw data with meaningful visualization. Bioimaging supports numerous biological discoveries, yet different techniques utilize distinct wavelength ranges to probe cellular components (Fig. 1A). Accurately visualizing this spectral information is crucial for interpretation. This study investigates the mathematical relationship between colorbars (Fig. 1B), chromaticity plots (Fig. 1C), and fluorescence intensity data mapped onto the RGB color space (Fig. 1D). While PixF was tailored to serve the purpose of this work, its generalizability as a reliable image processing platform when compared to ImageJ (and others) needs comprehensive benchmarking. Benchmarking against legacy tools like ImageJ is a lengthy endeavor. Therefore, preliminary soft benchmarking evidence for PixF was provided in the supplementary data (Figs. S2, S3, and Table S4)[29].

Colorbars and chromaticity

Colorbars (e.g., 'Rainbow') map numerical data to colours via defined colormaps. Chromaticity diagrams, such as the horseshoe-shaped plot (Fig. 1C), offer a framework for understanding this mapping. These plots represent perceivable colors through hue (color) and saturation (intensity). A colorbar sample points along specific paths in this chromaticity space. For example, the "Rainbow" colormap traverses a curved path encompassing hues from violet to red with increasing saturation towards the center.

Bioimaging and spectral ranges

Bioimaging techniques rely on fluorescence, where molecules emit light upon excitation at specific wavelengths. Different methods target various fluorophores with unique excitation and emission spectra. Confocal microscopy often utilizes 400–700 nm wavelengths, while Raman spectroscopy probes vibrational modes in the near-infrared range (700–1400 nm). Tools like PixF incorporate spectral spans to interpret fluorescent intensity data accurately. For example, applying a "Rainbow" colormap to Raman data may misrepresent information by exceeding the utilized wavelength range.

Mapping fluorescence to RGB

Fluorescence intensity data, measured in arbitrary units, requires conversion into RGB values for visualization. This mapping may use linear or non-linear functions to enhance contrast or emphasize features. Selecting an appropriate colormap significantly affects how fluorescence intensity variations translate into visual

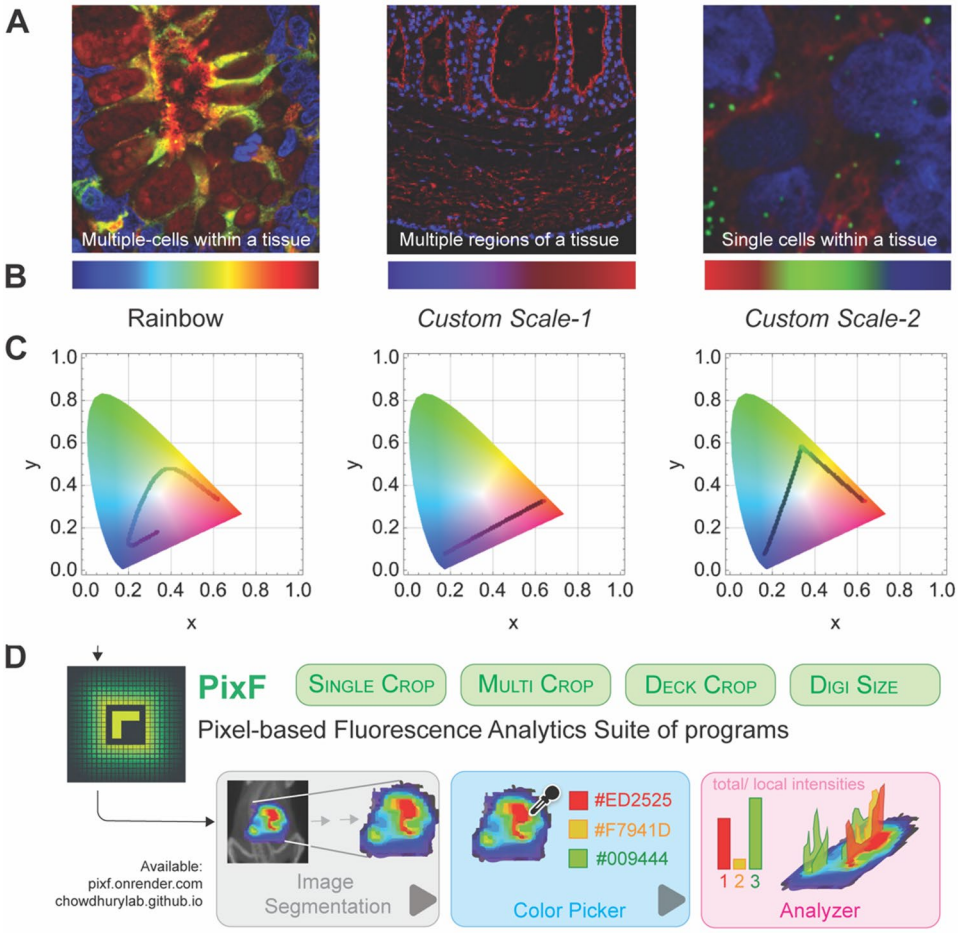

Fig. 1. PixF workflow—color scheme analysis, chromaticity mapping, and image segmentation modules. (**A**) PixF has been built to learn multiple color schemes used for different biological imaging experiments spanning scales of life. (**B**) By reasoning over the data, PixF can identify a color palette (albeit without directionality) where the user should indicate which end of the spectrum is high and which is low. (**C**) A chromaticity analysis enables projecting the travel of a color palette from a given image on the visible spectrum (convex hull). This is important for calculating the definitions of neighborhoods for a given color in the image. For example, Rainbow and Custom Scales have a larger travel and hence have a larger neighborhood for each color in comparison to FuchsiaTones. This means sensitivity towards variance in pixel-level intensity for FuchsiaTones must be stringent during PixF analysis. (**D**) Overview of the image segmentation, color picker (without a palette), and analyzer modules in PixF.

representations. While intuitive colormaps like "Rainbow" may lack precision, scientifically optimized colormaps such as "Viridis," "Inferno," "Plasma," and "Magma" (Matplotlib, v3.9.2)[30] provide perceptually accurate data visualization. Custom colormaps tailored to specific bioimaging applications further enhance interpretability.

3D bar plots for spatial molecular expression

The Python-based parsing module within PixF analyzes fluorescent images to quantify and visualize molecular expression across tissues. Images comprise red, green, and yellow channels, where yellow denotes overlapping red and green fluorescence regions. PixF splits images into individual channels, maps each pixel's location to the tissue region, and generates 3D bar plots. These plots map intensity values onto a normalized RGB scale, visually representing the spatial intensity of molecular expression in three dimensions.

3D bar plots facilitate the identification of differential molecular expression, highlighting tissue regions where one marker dominates at a pixel level. This capability uncovers spatial patterns of molecular activity, offering insights into viral infection mechanisms and tissue-specific entry points. Such quantifiable biological insights are critical for understanding how viruses affect host organs and tissues differently.

Availability of PixF through a web-based platform

PixF is a freely accessible web-based tool featuring an intuitive graphical user interface (GUI) that enables users to upload fluorescence data (red, green, and blue channel values) alongside acquisition details, such as excitation

and emission wavelengths. The platform applies mathematical transformations to map data into a relevant chromaticity space based on excitation/emission information, supports user-defined adjustments like mapping function fine-tuning and colormap selection optimized for specific applications, and generates high-resolution, publication-quality visualizations. By bridging raw fluorescence data with interpretable visual outputs, PixF democratizes access to advanced bioimage analysis tools, fostering deeper insights into bioimaging experiments. The tool is available at https://pixf.onrender.com/.

Statistical analysis

Respiratory and intestinal tissues from three animals and representative images were chosen and analyzed based on consistent staining intensity and structural integrity across replicates, as recommended[31,32]. Statistical analyses and plots were performed using GraphPad Prism® 10.6.0 (GraphPad Software Inc.). Total lectin staining intensity values were log10-transformed prior to analysis. A two-way ANOVA followed by Tukey's post hoc multiple comparisons test was used to evaluate differences in the labeling levels of three sialic acid (SA) types within the same tissue, as well as the labeling of a single SA across different tissues. For the individual immunofluorescence assays, log10-transformed total intensity values were analyzed using one-way ANOVA (within each receptor type), followed by Tukey's post hoc test to compare labeling levels across different tissues. For all analyses, a p-value < 0.05 was considered statistically significant.

Results

Sialic acid distribution in the respiratory tract

In the respiratory tract epithelium of beef cattle, SA α2,3-Galβ (1–3) receptors (*Maackia amurensis* lectin II, MAL II; red), specific for avian-origin IAVs, were predominantly expressed. MAL II staining was multifocal, primarily localized on the apical membrane of ciliated pseudostratified epithelial cells in the trachea and bronchi (Fig. 2A-C). MAL II labeling appeared more uniform and continuous in the lower respiratory tract, including the bronchioles and alveolar epithelium (Fig. 2D, E). Co-localized staining of MAL II and *Sambucus nigra* (SNA, SA α2,6-Gal; green), specific for mammalian-origin IAVs, was observed in mucus-secreting goblet cells (Fig. 2A- arrowheads), the cell membranes of basal cells (Fig. 2A- orange arrow), and within the submucosal glands (Fig. 2B). SNA labeling was predominantly confined to the subepithelial region, goblet cells, other glands, connective tissue, and interstitial spaces (Fig. 2A-E). Image analysis of MAL II and SNA co-expressing regions in the epithelial lining further revealed significantly higher levels of MAL II labeling (Fig. 2Aiii–Eiii). Notably, MAL I, specific for SA α2,3-Galβ (1–4) GlcNAc, was primarily localized to glandular regions and exhibited minimal to no labeling on the epithelial lining throughout the respiratory tract (Fig. 2F–J).

The labeling of SA N-glycolylneuraminic acid (Neu5Gc), as determined by IFA, was detected along the epithelial lining, particularly on the cell borders of ciliated pseudostratified epithelial cells in the trachea and within submucosal glands. Neu5Gc labeling was multifocally distributed along the epithelial lining of the bronchus, bronchioles, and cell membranes of alveoli (Fig. 2K–O).

Sialic acid distribution in the intestinal tract

The intestinal tract of beef cattle exhibited abundant SA α2,3-Gal receptors, with strong MAL I and MAL II binding in these regions (Fig. 3A–H). In contrast, SNA (SA α2,6-Gal) binding was predominantly localized to the subepithelial region (Fig. 3Ai) and goblet cells (Fig. 3Bi and Di). MAL I and MAL II co-labeling was observed on the epithelial lining of both the small (Fig. 3E) and large intestines (Fig. 3G), with MAL II demonstrating more robust labeling, as confirmed by PixF image analysis (Fig. 3Eiii–Hiii). The distribution of SA in goblet cells varied between the villus and crypt regions. MAL I labeling was stronger than MAL II in the goblet cells of the small intestine, and both lectins exhibited a consistent distribution pattern in goblet cells between the villus and crypt regions (Fig. 3E, F). In the large intestine, MAL I binding was more prominent in goblet cells on the apical or luminal side, whereas MAL II exhibited higher labeling in the crypt region (Fig. 3G, H).

The labeling of SA Neu5Gc was detected on both the villus epithelial membrane and goblet cells of the small intestine (Fig. 3I-J). However, its distribution in the large intestine was scattered, with minimal or no labeling observed on the epithelial lining (Fig. 3K, L).

Coronavirus receptors in respiratory and intestinal tracts

IFA revealed varied expression levels of coronavirus receptors (ACE2, TMPRSS2, APN, DPP4, and CEACAM1) in the bovine respiratory and intestinal tracts. Strong ACE2 expression was observed on the epithelial lining of the trachea, alveoli, and small and large intestines, with lower levels detected in the bronchus and bronchiole epithelium (Fig. 4A). TMPRSS2, APN, and DPP4 were widely expressed in the respiratory epithelium with a multifocal labeling, particularly evident in the alveoli. In the intestinal epithelium, TMPRSS2 and DPP4 were uniformly expressed in both villus and crypt regions, while APN exhibited comparatively lower levels of expression (Fig. 4B–D). CEACAM1 expression was limited in the respiratory tract, displaying a multifocal distribution, and was not detected in the intestinal tract (Fig. 4E).

Discussion

Recent outbreaks of highly pathogenic avian influenza A virus (HPAI H5N1) in dairy cattle have underscored the ability of viruses to adapt to new hosts, posing significant challenges to animal and human health. Cattle are susceptible to influenza C, influenza D, bovine coronavirus (BCoV), and SARS-CoV-2, affecting the respiratory and gastrointestinal systems.

Host infection begins with the virus binding to specific cellular receptors, a critical step for initiating the infection. IAVs utilize SA as key determinants for host cell attachment. These receptors also interact with other

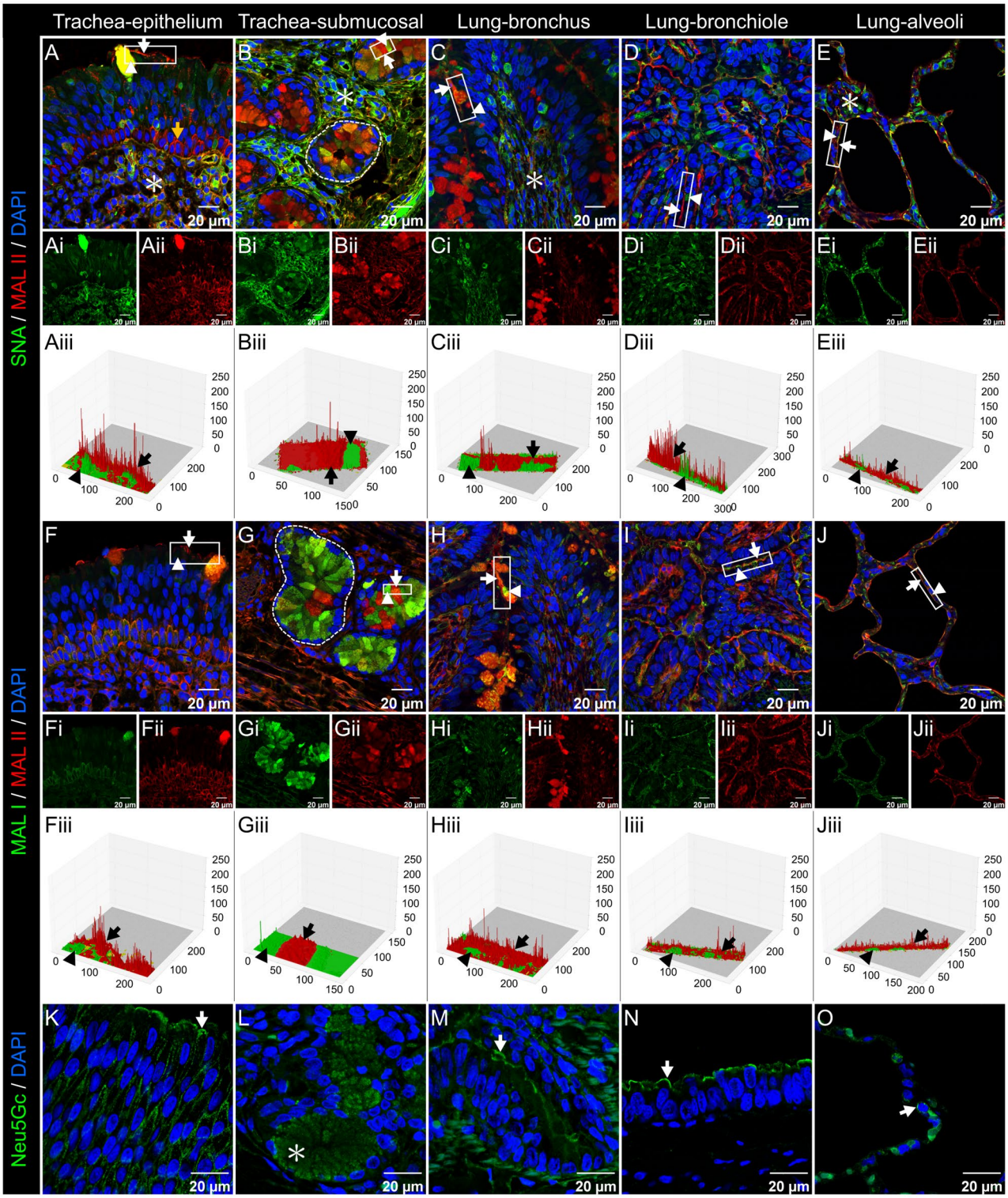

pathogens, including viruses, bacteria, fungi, and parasites[33–37]. Human and swine IAVs preferentially bind α2,6-linked SA (SA α2,6-Gal)[13,38,39], while avian and equine IAVs prefer α2,3-linked SA (SA α2,3-Gal)[9,40,41]. Pigs were traditionally considered "mixing vessels" due to the presence of both receptor types. However, it is now established that many species, including cattle, exhibit similar receptor diversity, thus broadening the potential range of intermediaries for reassortant IAVs[42].

Receptor distribution on cells varies significantly with age, sex, breed, health status, and tissue type. Additionally, antibody source, clone type, dilution, incubation, and imaging techniques used to study receptor distribution can influence the observed spatial distribution of the tissues analyzed. For instance, co-expression of receptors within the same cell or tissue region must be evaluated carefully. Particularly, dual staining with fluorescent dyes can lead to signal overlap caused by overlapping emission spectra, necessitating high-resolution methods like confocal microscopy. While tools like ImageJ are powerful, they often face challenges with

◀**Fig. 2**. Sialic acid distribution in the beef cattle respiratory tract. (**A**–**JJ**) Confocal microscopy images of fluorescently labeled lectins *Sambucus nigra* (SNA, FITC, green) specific for sialic acid (SA) α2,6-Gal, *Maackia amurensis* II (MAL II, DyLight 650, red) specific for SA α2,3-Galβ (1–3) GlcNAc, and *Maackia amurensis* I (MAL I, FITC, green) specific for SA α2,3-Galβ (1–4) GlcNAc. Blue represents nuclear staining using DAPI; scale bar = 20 µM. Representative merged images showing SNA/MAL II binding (**A**–**E**) and MAL I/MAL II binding (**F**–**J**). Multifocal, apical membranous (white arrow) MAL II labeling was observed on trachea epithelium and extensively on basal cells (orange arrow) (**A**), while goblet cells (arrowhead) showing intense cytoplasmic SNA (**Ai**) and MAL II (**Aii**) labeling. Image analysis of tracheal epithelial lining (3D plot of insert in **A**) showing greater MAL II labeling even in co-localized areas (arrow), and slightly higher SNA in goblet cell (arrowhead) (**Aiii**). Sub-mucosal areas showing both SNA and MAL II (**B**), with higher SNA in lamina propria connective tissue (asterisk) and higher MAL II in glands (dashed white outline). The 3D plot of insert in (**B**) demonstrated varying levels of expression of MAL II (arrow) and SNA (arrowhead) (**Biii**). Goblet cells and epithelial lining of the bronchus, bronchiole, and alveoli show intense MAL II labeling (arrow) (**C**, **D**, **E**) with SNA labeling in the lamina propria of the bronchus (white asterisk) (**C**) and the interstitial region of the alveolar wall (asterisk) (**E**). Quantitative image analysis confirmed that the lining of epithelial cells has higher membranous MAL II labeling (arrow) (**Ciii**, **Diii**, **Eiii**). MAL I demonstrated a labeling distribution analogous to that of MAL II, albeit with attenuated signal intensity (**F**, **H**–**J**), reflected in quantitative image analysis (**Fiii**, **Hiii**–**Jiii**). MAL I is more robust in the submucosal glands of the trachea (dashed white outline) (**G**, **Giii**). (**K**–**O**) Confocal images of the respiratory tract showing SA N-glycolylneuraminic acid (Neu5Gc, FITC, green) following immunofluorescence staining. Neu5Gc was detected on the apical membrane and cell borders of ciliated pseudostratified epithelia of the trachea (**K**), multifocally on the epithelial lining of the bronchus (**M**), bronchiole (**N**), and the alveoli (**O**). The sub-epithelial glands in the tracheal region also showed Neu5Gc (**L**).

efficiency and user-friendliness, especially when handling large datasets or conducting complex analyses[43]. These limitations underscore the need for advanced tools that are fast, intuitive, and capable of delivering accurate spatial quantification of fluorescent markers[44].

PixF, the pixel-based image analysis tool developed in this study, is positioned as a prototypic tool (i.e., beta version) to address these challenges by enabling a web-based rapid image processing tool that allows users to process images with intuitive segmentation, marker color picking, and batch processing of multiple images with a single click without compromising analysis quality. PixF offers applications beyond this study, including diagnostic pathology and radiology, where efficient image analysis can lead to faster diagnoses. The web-based nature of PixF makes it accessible to a broader range of researchers and clinicians, regardless of their computational resources or technical expertise. This pilot PixF implementation demonstrates how such an approach could lower entry barriers for image analysis, while recognizing that further validation is needed to assess its broader applicability. It is also positioned to be a practical onboarding tool for training entry-level students and learners to understand what a baseline image processing operation entails without requiring them to navigate the complexity of full-featured, professional-grade analysis suites thereby easing the entry barrier into computational image science. By eliminating artifacts such as bleed-through and non-specific fluorescence, PixF attempts to improve co-localization and spatial relationships between the two molecules, providing preliminary yet reliable data on receptor distribution and co-expression in tissue samples. A thorough fine-grained benchmarking endeavor is underway. The performance metrics of PixF with respect to ImageJ were detailed in supplementary data (Figs. S2, S3, and Table S4).

Using high-resolution confocal imaging and PixF analysis, this preliminary implementation explored the spatial distribution of IAV and CoV receptors in bovine respiratory and intestinal tracts (Fig. 5). The predominant presence of SA α2,3-Galβ (1–3) (MAL II) on epithelial linings indicates a strong affinity for avian-origin IAVs such as HPAI H5N1[45–47]. Co-localization of SA α2,6-Gal and SA α2,3-Galβ (1–3) in goblet cells and submucosal glands suggests dual susceptibility to avian and mammalian IAVs. However, the restricted expression of SA α2,6-Gal to subepithelial regions indicates a limited role for mammalian IAVs in cattle. Differential MAL I and MAL II distribution in goblet cells across villus and crypt regions, as observed in pigs[38], highlights specialized roles in mucosal immunity and pathogen interaction.

SAs also act as receptors or co-receptors for CoVs. Neu5Gc, a prominent SA in cattle, has been associated with human gut inflammation and serves as a co-receptor for CoVs[48]. Its scattered distribution in respiratory and intestinal tissues suggests complex roles in viral binding and immunity, warranting further investigation.

CoVs rapidly adapt to new hosts through high mutation rates, frequent recombination events, and large genomes[49]. Recent examples include CCoV-HuPn-2018 using APN[50] and HKU1 using TMPRSS2[51] as functional receptors for cell entry. BCoV, which causes pneumonia and enteritis in cattle, is also thought to play a role in bovine respiratory disease complex (BRDC)[4], a condition responsible for significant economic losses worldwide due to substantial morbidity and mortality. This pneumoenteric virus belongs to the genus *Betacoronavirus*, a genus that is highly variable and uses different protein receptors to attach to host cells[52], ACE2 (SARS-CoV)[53,54], TMPRSS2 (HKU1)[51], DPP4 (Middle East respiratory syndrome coronavirus; MERS-CoV)[25,55,56], CEACAM1 (mouse hepatitis virus -MHV)[57], and SA 5-N-acetyl-9-O-acetylneuraminic acid (Neu5,9Ac_2; Human coronaviruses strain OC43, HCoV-OC43)[58]. BCoV also uses SAs as attachment factors, but is not essential for infection[59]. Several bovine-like CoVs isolated from wild and captive ruminants exhibit biological, antigenic, and genetic similarities to BCoV[4]. Although the exact ancestral strain has not been identified, it is assumed that some of these similarities may stem from recombination events involving BCoV. It is postulated that BCoV may have adapted to a human host, resulting in the emergence of HCoV-OC43[60]. Interestingly, the SARS-CoV-2

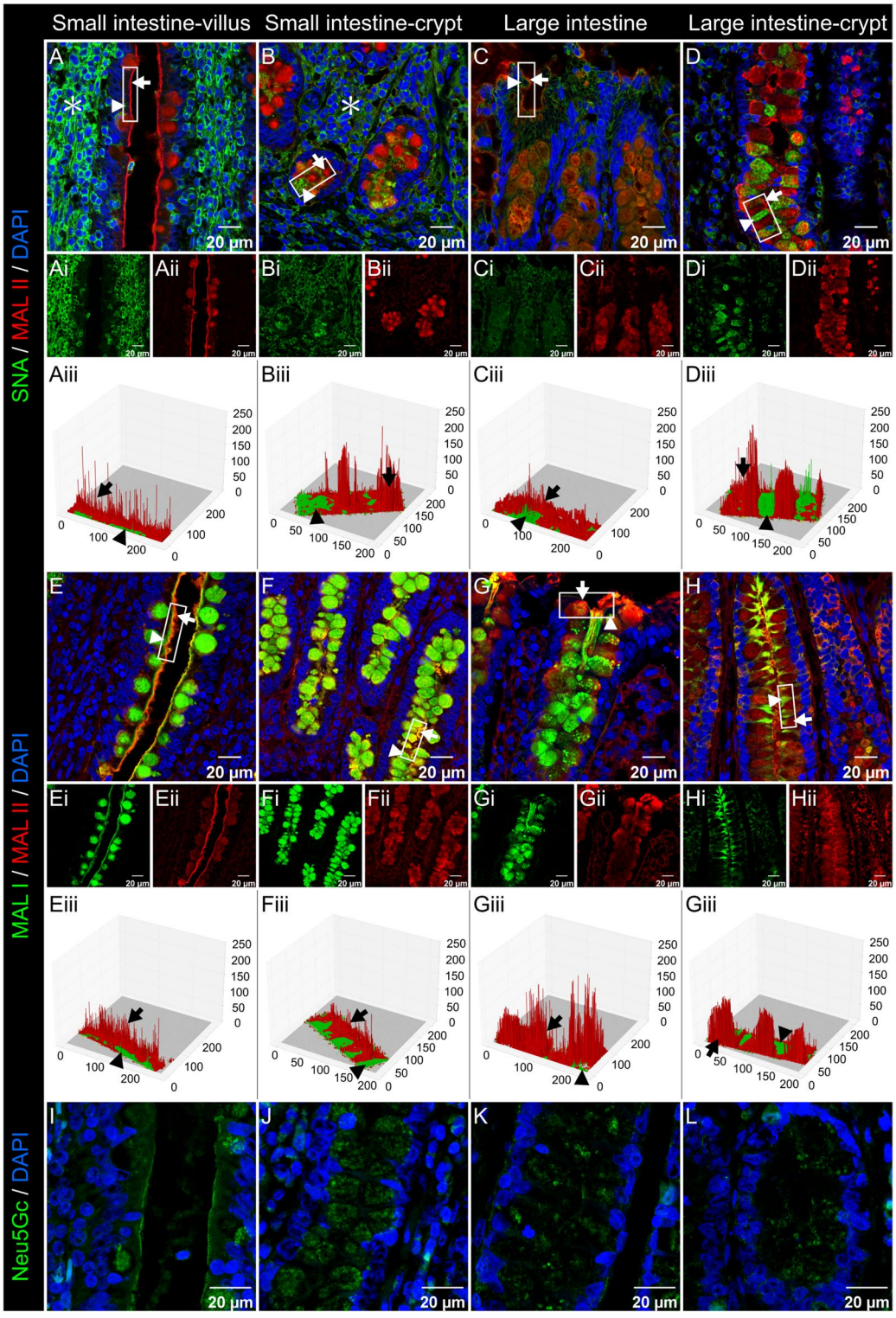

virus, a *Betacoronavirus*, is known to have affected a wide range of domestic, captive, and wild animals along with humans[26]. To address some of these transmission events and the role of cattle, it is crucial to evaluate the host susceptibility factors, including the coronavirus receptors in bovine respiratory and intestinal tracts, which are the predilection sites.

The protein expression of CoV receptors (ACE2, TMPRSS2, APN, DPP4, and CEACAM1) was mapped on tissues in this study, including gene expression (Supplementary Table S2 and S3). Strong ACE2 expression was detected in the trachea, alveoli, and intestinal epithelium, while TMPRSS2 and DPP4 were uniformly expressed across villi and crypt regions. Previous studies had similar ACE2 expression levels in the 18-month-old bovine trachea[61]. APN expression was higher in respiratory tissues but comparatively lower in the intestinal epithelium, differing from previous findings in calves that reported strong APN expression in bronchiole[62] the intestinal lining[63]. Sparse CEACAM1 expression in respiratory tissues and its absence in the intestinal tract

◀**Fig. 3**. Sialic acid distribution in the beef cattle intestinal tract. (A-H) Confocal microscopy images of fluorescently labeled lectins *Sambucus nigra* (SNA, FITC, green) specific for sialic acid (SA) α2,6-Gal, *Maackia amurensis* II (MAL II, DyLight 650, red) specific for SA α2,3-Galβ (1–3) GlcNAc, and *Maackia amurensis* I (MAL I, FITC, green) specific for SA α2,3-Galβ (1–4) GlcNAc. Blue represents nuclear staining using DAPI; scale bar = 20 μM. Representative merged images showing SNA/MAL II binding (**A**–**D**) and MAL I/MAL II binding (**E**–**H**). The epithelial lining of the small and large intestine shows MAL II labeling (insets of **A**, **C**), which was evident in the quantitative image analysis (arrow) (**Aiii**, **Ciii**). Goblet cells located in the crypt and apical region of the intestines show abundant MAL II labeling (**A**–**D**). SNA labeling was limited to lamina propria (asterisk) (**A**, **B**) and goblet cells in the crypt region of the intestines (arrowhead) (**B**, **D**). MAL I and MAL II were labeled largely co-localized (**E**–**H**) in both the epithelial lining and goblet cells. Quantitative image analysis indicates MAL II was comparatively higher in the co-localized areas (arrow) (insets of **E**, **G**, **Eiii**, **Giii**). Uniform labeling of MAL I in goblet cells distributed toward apical or crypt regions of the small intestine (**Ei**, **Fi**). Note the gradient decrease in MAL I labeling in the goblet cells distributed toward the apical to crypt regions of the large intestine (**Gi**, **Hi**). (**I**–**L**) Confocal images of small and large intestines showing SA N-glycolylneuraminic acid (Neu5Gc, FITC, green) following immunofluorescence staining. The SA Neu5Gc was expressed on the epithelial lining and goblet cells of the small intestine (**I**, **J**). Neu5Gc expression was more scattered in the large intestine, and there was no evident expression on the epithelial lining (**K**, **L**).

may reflect the low cross-reactivity of the human antibody used, a technical limitation (Supplementary Table S1). CEACAM1 is the receptor for MHV[64] and so far, there is no evidence showing CEACAM1 as a functional receptor for other coronaviruses, even though the BCoV and MHV spike protein N-terminal domains share high homology[65]. These findings highlight varied receptor distribution across tissues, with potential implications for viral attachment and host-pathogen interactions. This study is the first to report the spatial distribution of TMPRSS2, DPP4, and CEACAM1 in bovine respiratory and intestinal tract epithelium. While the coronavirus receptors evaluated in this study are predominantly localized to the apical membrane of epithelial cells, mediating viral entry, the cytoplasmic signals observed in the confocal images may reflect receptor presence within intracellular compartments, including organelle membranes, and are consistent with dynamic processes such as protein trafficking[66,67]. Variations in receptor expression across tissues and PixF's ability to quantify co-localized staining provide novel and early insights into the roles of receptors in viral attachment and host susceptibility. These findings provide an initial demonstration of how PixF can facilitate high-throughput image-based analysis, warranting further validation and refinement in future studies. While PixF can quantify spatial distribution patterns of fluorescence signals, it does not independently resolve subcellular localization. We recognize this as a current limitation of this approach, consistent with the pilot nature of this study, which aims to assess PixF's potential utility. Accurate interpretation of localization data requires integration with established knowledge of protein biology and cellular context to avoid overinterpretation of distribution metrics alone. Although Neu5,9Ac2 was not mapped, future studies using alternative methods could elucidate its role in BCoV attachment and replication[68].

In summary, this study highlights the rich presence of IAV and CoV receptors in bovine respiratory and intestinal tracts, with varying abundances depending on tissue type and region. Tools like PixF lays the foundation of a fully web-based, easy-to-use framework, that minimizes the number of clicks, for translating complex image data into actionable insights, contributing to the understanding of viral entry, attachment, and tissue trophism.

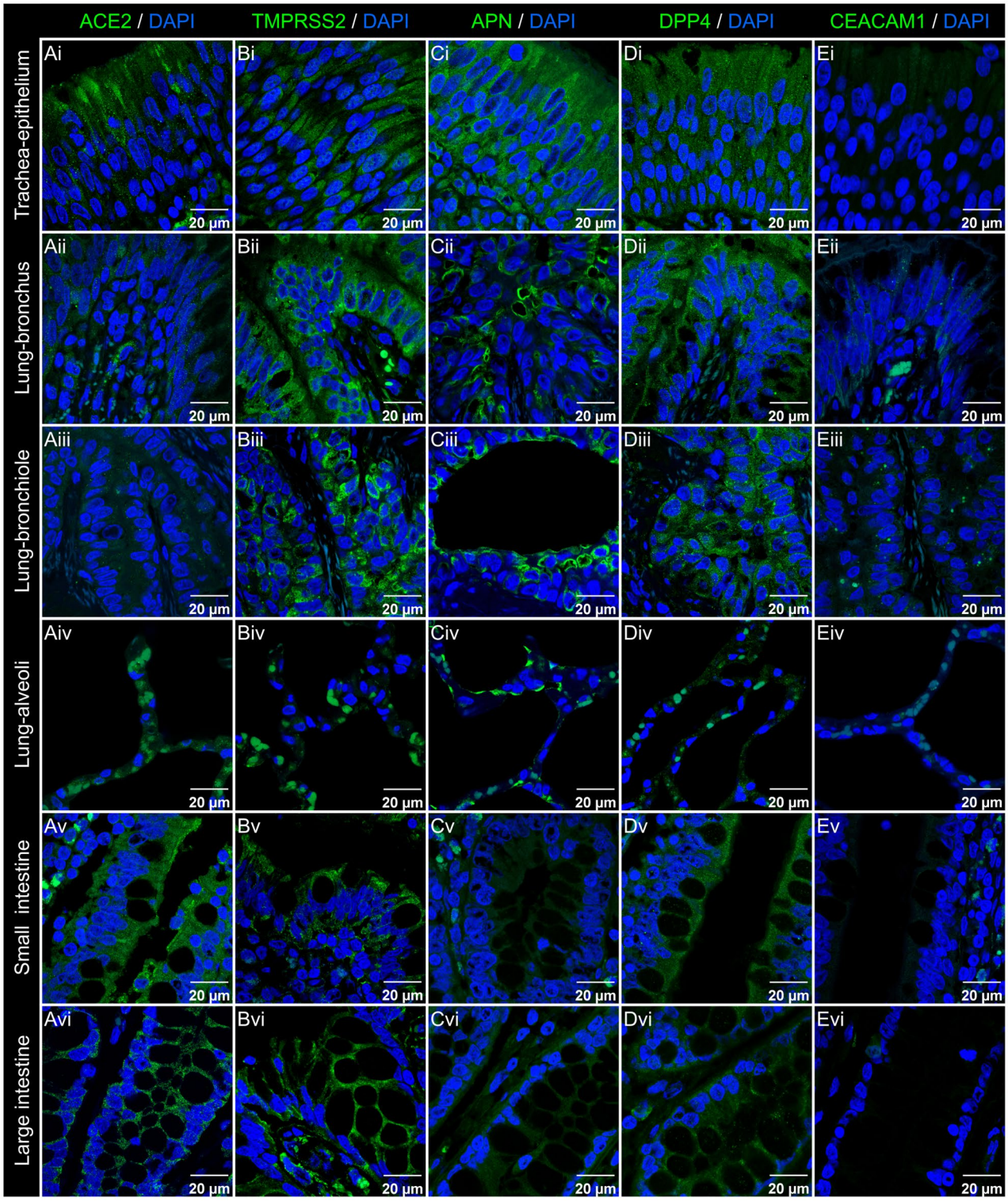
ACE2 / DAPI
TMPRSS2 / DAPI
APN / DAPI
DPP4 / DAPI
CEACAM1 / DAPI
Trachea-epithelium
Lung-bronchus
Lung-bronchiole
Lung-alveoli
Small intestine
Large intestine
Ai
Bi
Ci
Di
Ei
Aii
Bii
Cii
Dii
Eii
Aiii
Biii
Ciii
Diii
Eiii
Aiv
Biv
Civ
Div
Eiv
Av
Bv
Cv
Dv
Ev
Avi
Bvi
Cvi
Dvi
Evi
20 μm

◀**Fig. 4**. Coronavirus receptors in the respiratory tract and intestinal tracts of beef cattle. Confocal images showing angiotensin-converting enzyme 2 (ACE2, **A**), transmembrane protease serine 2 (TMPRSS2, **B**), aminopeptidase N (APN, **C**), dipeptidyl peptidase 4 (DPP4, **D**), and carcinoembryonic antigen-related cell adhesion molecule 1 (CEACAM1, **E**) expression following immunofluorescence staining. Primary antibodies, ACE2 (4 µg/ml, Cat# sc-390851), TMPRSS2 (0.2 µg/ml; Cat# sc-515727), APN (0.16 µg/ml; Cat# sc-166105), CEACAM1 (4 µg/ml; Cat# sc-166453), and DPP4 (1:50 dilution; Cat# BOV2078, Washington State University Monoclonal Antibody Center, Pullman, WA, USA); Secondary antibody, AffiniPure™ Donkey Anti-Mouse IgG (H + L) conjugated Alexa Fluor® 488 (15 µg/ml; Cat# 715-545-150). Blue represents nuclear staining using DAPI; scale bar = 20 µM. Representative images of coronavirus receptor expression across tissues are shown. The epithelial lining of the trachea (**Ai**), alveoli (**Aiv**), small intestine (**Av**), and large intestine (**Avi**) showed strong ACE2 expression compared to the bronchus (**Aii**) and bronchiole (**Aiii**). The respiratory epithelium showed extensive TMPRSS2, APN, and DPP4 expression with a multifocal expression on the alveoli (**Bi**–**iv**, **Ci**–**iv**, **Di**–**iv**). TMPRSS2 (**Bv**–**vi**) and DPP4 (**Dv**–**vi**) were detected uniformly on villi and crypt regions in the small and large intestine epithelia, while APN levels were comparatively low in both intestines (**Cv**–**vi**). With the exception of the bronchus (**Eii**) and bronchiole (**Eiii**), the levels of CEACAM1 were low to no detection on the epithelia of all the tissues assessed (**Ei**, **Eiv**–**vi**).

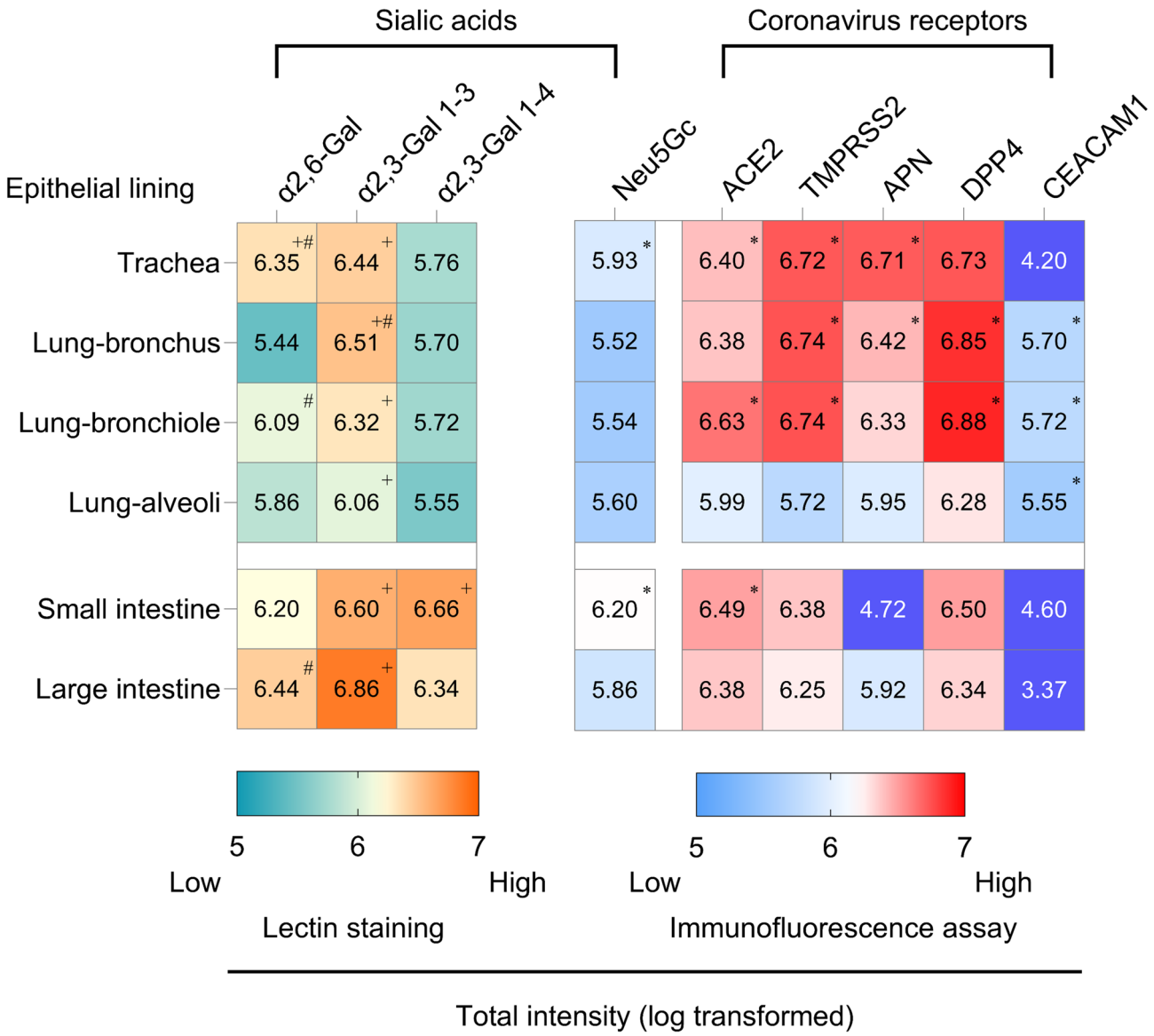

Fig. 5. Heat map showing the distribution of influenza and coronavirus receptors in the respiratory and intestinal tracts of beef cattle. Heatmap was generated using data from PixF image analysis showing the average $\log_{10}$ total intensity (sum of intensity in all the pixels with signal) of cropped images ($n = 3$) by a 350*350-pixel region of interest (ROI) on the epithelium of respiratory and intestinal tract tissues. The color scale of lectin staining (orange, high; light yellow, medium; green, low) and immunofluorescence assay (red, high; white, medium; blue, low; dark blue < 5) indicates the level of log total intensity. ACE2, angiotensin-converting enzyme 2; TMPRSS2, transmembrane protease serine 2; APN, aminopeptidase N; DPP4, dipeptidyl peptidase 4; CEACAM1, carcinoembryonic antigen-related cell adhesion molecule 1. Respiratory and intestinal tissues were analyzed separately. For lectin staining data was analyzed with two-way ANOVA, and multiple comparisons with post hoc Tukey test. The levels of sialic acids within the same tissue ($^{+}$denotes significant higher with $P < 0.05$) and one SA across different tissues ($^{\#}$denotes significant higher with $P < 0.05$). Immunofluorescence assay was analyzed with one-way ANOVA (within the same receptor), and multiple comparison with post hoc Tukey test was conducted to compare between different tissues (*denotes significant higher with $P < 0.05$).

Data availability

The datasets generated and/or analyzed during the current study are available in the GitHub repository: [https://github.com/ChowdhuryRatul/pixf-channel-analysis]

Received: 14 December 2024; Accepted: 11 November 2025
Published online: 17 December 2025

References

1. WHO. Coronavirus disease (COVID-19). Similarities and differences between COVID-19 and Influenza. *World health Organisation* 2–5 (2021). https://www.who.int/emergencies/diseases/novel-coronavirus-2019/question-and-answers-hub/q-a-detail/coronavirus-disease-covid-19-similarities-and-differences-with-influenza
2. The 1918 Flu. and COVID-19: A Tale of Two Pandemics | NIH Intramural Research Program. https://irp.nih.gov/catalyst/29/2/the-1918-flu-and-covid-19-a-tale-of-two-pandemics
3. Vlasova, A. N. et al. Porcine coronaviruses. *Emerg. Transbound. Anim. Viruses*, 1st ed. 79–110 (Singapore, Springer, 2020). https://doi.org/10.1007/978-981-15-0402-0_4.
4. Vlasova, A. N. & Saif, L. J. Bovine coronavirus and the associated diseases. *Front. Vet. Sci.* **8**, 643220 (2021).
5. Phelan, A. L. et al. COVID-19 has left the world less prepared for an influenza pandemic. *Nat. Med.* **29**, 1044–1045 (2023).
6. Webby, R. J., Webster, R. G. & Richt, J. A. Influenza viruses in animal wildlife populations. *Curr. Top. Microbiol. Immunol.* **315**, 67–83 (2007).
7. Ghai, R. R. et al. Animal reservoirs and hosts for emerging alphacoronaviruses and betacoronaviruses. *Emerg. Infect. Dis.* **27**, 1015–1022 (2021).
8. Drake, J. W. & Holland, J. J. Mutation rates among RNA viruses. *Proc. Natl. Acad. Sci. U S A.* **96**, 13910–13913 (1999).
9. Suzuki, Y. et al. Sialic acid species as a determinant of the host range of influenza A viruses. *J. Virol.* **74**, 11825–11831 (2000).
10. Arruda, B. et al. Divergent pathogenesis and transmission of highly pathogenic avian influenza A(H5N1) in swine. *Emerg. Infect. Dis.* **30**, 738–751 (2024).
11. Nicholls, J. M., Chan, R. W. Y., Russell, R. J., Air, G. M. & Peiris, J. S. M. Evolving complexities of influenza virus and its receptors. *Trends Microbiol.* **16**, 149–157 (2008).
12. Venkatesh, D. et al. Antigenic characterization and pandemic risk assessment of North American H1 influenza A viruses circulating in swine. *Microbiol. Spectr.* **10**, e01781–e01722 (2022).
13. Shinya, K. et al. Influenza virus receptors in the human airway. *Nature* **440**, 435–436 (2006).
14. Nguyen, L. et al. Sialic acid-containing glycolipids mediate binding and viral entry of SARS-CoV-2. *Nat. Chem. Biol.* **18**, 81–90 (2022).
15. Tan, C. W. et al. Cell surface α2,3-linked Sialic acid facilitates Zika virus internalization. *Emerg. Microbes Infect.* **8**, 426–437 (2019).
16. Taube, S. et al. Ganglioside-linked terminal Sialic acid moieties on murine macrophages function as attachment receptors for murine Noroviruses. *J. Virol.* **83**, 4092–4101 (2009).
17. Haselhorst, T. et al. Sialic acid dependence in rotavirus host cell invasion. *Nat. Chem. Biol.* **5**, 91–93 (2009).
18. Huang, L. Y. et al. Characterization of the Adeno-associated virus 1 and 6 Sialic acid binding site. *J. Virol.* **90**, 5219 (2016).
19. Arnberg, N., Edlund, K., Kidd, A. H. & Wadell, G. Adenovirus type 37 uses Sialic acid as a cellular receptor. *J. Virol.* **74**, 42–48 (2000).
20. O'Hara, S. D., Stehle, T. & Garcea, R. Glycan receptors of the polyomaviridae: structure, function, and pathogenesis. *Curr. Opin. Virol.* **7**, 73–78 (2014).
21. Stuart, A. D. & Brown, T. D. K. α2,6-linked Sialic acid acts as a receptor for feline calicivirus. *J. Gen. Virol.* **88**, 177–186 (2007).
22. Yan, R. et al. Structural basis for the recognition of SARS-CoV-2 by full-length human ACE2. *Sci. (1979).* **367**, 1444–1448 (2020).
23. Delmas, B. et al. Aminopeptidase N is a major receptor for the enteropathogenic coronavirus TGEV. *Nature* **357**, 417–420 (1992).
24. Williams, R. K., Jiang, G., Sen & Holmes, K. V. Receptor for mouse hepatitis virus is a member of the carcinoembryonic antigen family of glycoproteins. *Proc. Natl. Acad. Sci. U S A.* **88**, 5533–5536 (1991).
25. Raj, V. S. et al. Dipeptidyl peptidase 4 is a functional receptor for the emerging human coronavirus-EMC. *Nature* **495**, 251–254 (2013).
26. Zhuang, J., Yan, Z., Zhou, T., Li, Y. & Wang, H. The role of receptors in the cross-species spread of coronaviruses infecting humans and pigs. *Arch. Virol.* **169**, 1–11 (2024).
27. Smallcombe, A. Multicolor imaging: the important question of co-localization. *Biotechniques* **30**, 1240–1246 (2001).
29. Lin, S. J. H., Helm, E. T., Gabler, N. K. & Burrough, E. R. Acute infection with Brachyspira hyodysenteriae affects mucin expression, glycosylation, and fecal MUC5AC. *Front Cell. Infect. Microbiol* **12**, 1042815. https://doi.org/10.3389/fcimb.2022.1042815 (2023).
30. Hitrec, T. et al. Neural control of fasting-induced torpor in mice. *Sci. Rep* **9**(1), 15462. https://doi.org/10.1038/s41598-019-51841-2 (2019). Erratum in: *Sci. Rep.* **10**(1), 4263. https://doi.org/10.1038/s41598-020-61223-8 (2020).
30. Colormap reference. — Matplotlib 3.8.2 documentation. https://matplotlib.org/3.8.2/gallery/color/colormap_reference.html
31. Taylor, C. R. & Levenson, R. M. Quantification of immunohistochemistry—issues concerning methods, utility and semiquantitative assessment II. *Histopathology* **49**, 411–424 (2006).
32. Walker, R. A. Quantification of immunohistochemistry—issues concerning methods, utility and semiquantitative assessment I. *Histopathology* **49**, 406–410 (2006).
33. Hopkins, A. P., Hawkhead, J. A. & Thomas, G. H. Transport and catabolism of the Sialic acids N-glycolylneuraminic acid and 3-keto-3-deoxy-d-glycero-d-galactononononic acid by Escherichia coli K-12. *FEMS Microbiol. Lett.* **347**, 14–22 (2013).
34. Eneva, R., Engibarov, S., Abrashev, R., Krumova, E. & Angelova, M. Sialic acids, sialoconjugates and enzymes of their metabolism in fungi. *Biotechnol. Biotechnol. Equip.* **35**, 364–375 (2021).
35. Cavalcante, T., Medeiros, M. M., Mule, S. N., Palmisano, G. & Stolf, B. S. The role of Sialic acids in the establishment of infections by Pathogens, with special focus on leishmania. *Front. Cell. Infect. Microbiol.* **11**, 671913 (2021).
36. Warwas, M. L., Watson, J. N., Bennet, A. J. & Moore, M. M. Structure and role of Sialic acids on the surface of Aspergillus fumigatus conidiospores. *Glycobiology* **17**, 401–410 (2007).
37. Ezekiel, R. et al. Sialic acids in health and disease. *Biologics*. **5**, 10 (2025).
38. Nelli, R. K. et al. Comparative distribution of human and avian type Sialic acid influenza receptors in the pig. *BMC Vet. Res.* **6**, 4 (2010).
39. Van Riel, D. et al. Human and avian influenza viruses target different cells in the lower respiratory tract of humans and other mammals. *Am. J. Pathol.* **171**, 1215–1223 (2007).
40. Costa, T. et al. Distribution patterns of influenza virus receptors and viral attachment patterns in the respiratory and intestinal tracts of seven avian species. *Vet. Res.* **43**, 28 (2012).
42. Kuchipudi, S. V. et al. Differences in influenza virus receptors in chickens and ducks: implications for interspecies transmission. *J. Mol. Genet. Med.* **3**(1), 143–151. https://doi.org/10.4172/1747-0862.1000026 (2009).
42. Butt, S. L., Nooruzzaman, M., Covaleda, L. M. & Diel, D. G. Hot topic: influenza A H5N1 virus exhibits a broad host range, including dairy cows. *JDS Commun.* **5**, S13–S19 (2024).
44. Dietz, C. et al. Integration of the ImageJ ecosystem in the KNIME analytics platform. *Front Comput. Sci.* **2**, 8. https://doi.org/10.3389/fcomp.2020.00008 (2020).
44. Khadatare, M. & nvImageCodec (eds) | NVIDIA. (2024). https://developer.nvidia.com/blog/advancing-medical-image-decoding-with-gpu-accelerated-nvimagecodec/
45. Suzuki, Y. Sialobiology of influenza: molecular mechanism of host range variation of influenza viruses. *Biol. Pharm. Bull.* **28**, 399–408 (2005).
46. Ríos Carrasco, M., Gröne, A., van den Brand, J. M. A. & de Vries, R. P. The mammary glands of cows abundantly display receptors for Circulating avian H5 viruses. *J. Virol.* https://doi.org/10.1128/JVI.01052-24 (2024).
48. Nelli, R. K. et al. Sialic acid receptor specificity in mammary gland of dairy cattle infected with highly pathogenic avian influenza A(H5N1) virus. *Emerg. Infect. Dis.* **30**(7), 1361–1373. https://doi.org/10.3201/eid3007.240689 (2024).

49. Jahan, M., Thomson, P. C., Wynn, P. C. & Wang, B. The non-human glycan, N-glycolylneuraminic acid (Neu5Gc), is not expressed in all organs and skeletal muscles of nine animal species. *Food Chem.* **343**, 128439. https://doi.org/10.1016/j.foodchem.2020.128439 (2021).
49. Woo, P. C. Y., Lau, S. K. P., Huang, Y. & Yuen, K. Y. Coronavirus diversity, phylogeny and interspecies jumping. *Exp. Biol. Med.* **234**, 1117–1127 (2009).
50. Tortorici, M. A. et al. Structure, receptor recognition, and antigenicity of the human coronavirus CCoV-HuPn-2018 Spike glycoprotein. *Cell* **185**, 2279–2291e17 (2022).
51. Saunders, N. et al. TMPRSS2 is a functional receptor for human coronavirus HKU1. *Nature*. **624**, 207–214 (2023).
52. Parkhe, P. & Verma, S. Evolution, interspecies transmission, and zoonotic significance of animal coronaviruses. *Front. Vet. Sci.* **8**, 719834 (2021).
53. Li, W. et al. Angiotensin-converting enzyme 2 is a functional receptor for the SARS coronavirus. *Nature*. **426**, 450–454 (2003).
54. Lean, F. Z. X. et al. Differential susceptibility of SARS-CoV-2 in animals: evidence of ACE2 host receptor distribution in companion animals, livestock and wildlife by immunohistochemical characterisation. *Transbound. Emerg. Dis.* **69**, 2275–2286 (2022).
55. Widagdo, W. et al. Tissue distribution of the MERS-Coronavirus receptor in bats. *Sci. Rep.* **7**, 1–8 (2017).
56. Vergara-Alert, J. et al. Livestock susceptibility to infection with middle east respiratory syndrome Coronavirus - 23, number 2—February 2017 - emerging infectious diseases journal - CDC. *Emerg. Infect. Dis.* **23**, 232–240 (2017).
57. Dveksler, G. S. et al. Several members of the mouse carcinoembryonic antigen-related glycoprotein family are functional receptors for the coronavirus mouse hepatitis virus-A59. *J. Virol.* **67**, 1 (1993).
58. Hulswit, R. J. G. et al. Human coronaviruses OC43 and HKU1 bind to 9-O-acetylated Sialic acids via a conserved receptor-binding site in Spike protein domain A. *Proc. Natl. Acad. Sci. U S A*. **116**, 2681–2690 (2019).
59. Szczepanski, A. et al. Canine respiratory coronavirus, bovine coronavirus, and human coronavirus OC43: receptors and attachment factors. *Viruses 2019*. **11, Page 328** (11), 328 (2019).
60. Vijgen, L. et al. Complete genomic sequence of human coronavirus OC43: molecular clock analysis suggests a relatively recent zoonotic coronavirus transmission event. *J. Virol.* **79**, 1595–1604 (2005).
61. Di Teodoro, G. et al. SARS-CoV-2 replicates in respiratory ex vivo organ cultures of domestic ruminant species. *Vet. Microbiol.* **252**, 108933 (2021).
62. Lean, F. Z. X. et al. Distribution of aminopeptidase N coronavirus receptors in the respiratory and digestive tracts of domestic and wild artiodactyls and carnivores. *J. Gen. Virol.* **106**, 2092 (2025).
63. Landsverk, T. Histochemical distribution of enzymes in the small intestine of young Milk-Fed calves. *Acta Vet. Scand.* **21**, 402 (1980).
64. Taguchi, F. & Hirai-Yuki, A. Mouse hepatitis virus receptor as a determinant of the mouse susceptibility to MHV infection. *Front. Microbiol.* **3**, 21270 (2012).
65. Peng, G. et al. Crystal structure of bovine coronavirus Spike protein lectin domain. *J. Biol. Chem.* **287**, 41931–41938 (2012).
66. Danielsen, E. M., Hansen, G. H. & Niels-Christiansen, L. L. Localization and biosynthesis of aminopeptidase N in pig fetal small intestine. *Gastroenterology* **109**, 1039–1050 (1995).
67. Badawi, S. & Ali, B. R. ACE2 Nascence, trafficking, and SARS-CoV-2 pathogenesis: the Saga continues. *Hum. Genomics*. **15**, 1–14 (2021).
68. Wasik, B. R. et al. Distribution of O-acetylated sialic acids among target host tissues for influenza virus. *mSphere* 2, (2017).

Acknowledgements

We thank Michael Holtzbauer at Meat Lab, Iowa State University, Lu Yen, Charlotte Barnes, Brooklyn Elwood, and Isabella Jaspering for their help in collecting the tissue samples. The authors would like to thank Jennifer M Groeltz-Thrush, Haley Marie Lambert, Linda Sue Smith, and other veterinary diagnostic laboratory histology staff at Iowa State University for their timely processing of histology samples. We are incredibly thankful to Margie Carter from ISU - Roy J. Carver High-Resolution Microscopy Facility for helping us with Confocal microscopy imaging. Beta testing of PixF, presented in the supplementary information, was done by students of CHE 440/540 at Iowa State University, taught by R.C. They were patient enough to tolerate a buggy platform. The authors would like to thank Rahil Salehi for helping with editing the paper.

Author contributions

Conceptualization, R.K.N., R.C., L.G.L.; Methodology, N.C.T., Y.C.T., C.P.H.T., X.C., R.D., R.E.P., L.G.L., R.C., R.K.N.; Software development, Y.C.T., C.P.H.T., R.D., R.C.; Validation, T.B., R.K.N., R.C.; Formal analysis, N.C.T., Y.C.T., R.D., R.C., R.K.N.; Investigation, N.C.T., Y.C.T., R.C., R.K.N.; Resources, R.K.N., R.C., L.G.L., R.E.P.; Data curation, N.C.T., Y.C.T., R.D., R.C., R.C., R.K.N.; Writing (original draft preparation), N.C.T., Y.C.T., R.C., R.K.N.; Writing-review and editing, N.C.T., Y.C.T., C.P.H.T., X.C., R.E.P., L.G.L., R.C., R.K.N.; Visualization, N.C.T., Y.C.T., R.C., R.K.N.; Supervision, L.G.L., R.C., R.K.N., Funding acquisition, R.C., R.K.N.

Funding

The work is partly funded by Iowa State University Foundation grants and funds generated through fee-for-service projects to R.K.N. This work is also partially supported by the Iowa State University Startup Grant, Iowa State University Vice President of Research Seed Grant, Iowa Economic Development Authority Award Number: 24IEC006, and NSF 22–599, EPSCoR RII Track-1, Award Number DQDBM7FGJPC5 to R.C.

Declarations

Competing interests

The authors declare no competing interests.

Additional information

Supplementary Information The online version contains supplementary material available at https://doi.org/10.1038/s41598-025-28429-0.

Correspondence and requests for materials should be addressed to R.C. or R.K.N.